Micromechanical Properties Assessment of Slag Blended Cements Using Nanoindentation and Scanning Electron Microscopy

Imane Bekrine, Benoit Hilloulin, Ahmed Loukili

Micromechanical properties assessment of slag blended cements using nanoindentation and scanning electron microscopy

Imane Bekrine, Benoit Hilloulin[0000-0002-3668-6724] and Ahmed Loukili

Nantes Université, Ecole Centrale Nantes, CNRS, Institut de Recherche en Génie Civil et Mécanique (GeM), UMR 6183, F-44000 Nantes, France
imane.bekrine@ec-nantes.fr

Abstract. Sustainability concerns related to the CO_2 emissions of Portland cement production led to the exploitation of some by-products as replacement materials, such as slag. This requires a good understanding of the blended cementitious materials at the microscale to fully explain the observed behavior of the structures at the macroscale. The nanoindentation technique was used to assess the effect of slag incorporation on the micromechanical properties at the early age through the study of four cement pastes with different replacement ratios. Then, the nanoindents were observed using scanning electron microscopy to address the issues related to nanoindentation data deconvolution. The results show that the hydration products are intimately intermixed and that the boundary condition of indented areas must be considered when assessing the properties of individual phases to reduce the measurement variability. In addition, the incorporation of slag was found to cause a decrease in hydration products' elastic modulus and creep properties due to the gel porosity increase.

Keywords: Nanoindentation, SEM, Cement paste, Slag, micromechanical properties.

1 Introduction

The use of supplementary cementitious materials as a partial replacement for Portland cement is one of the most feasible and effective solution for producing more sustainable concretes. The exploitation of some by-products such as fly ash, silica fume and slag was proven to be beneficial, not only to mitigate the environmental problem of solid waste management, but also to improve the mechanical behavior and durability of cementitious materials, either by pozzolanic activity [1,2] or additional hydraulic reactions [3]. Nonetheless, the replacement of high amounts of Portland cement is still not very applicable because of the low understanding of the binding phase microstructure.

The understanding of blended cement pastes microstructures was massively addressed using different techniques such as X-ray diffraction (XRD), thermogravimetric analysis (TGA), mercury intrusion porosimetry (MIP), or also imaging techniques

such as scanning and transmission electron microscopy (TEM and SEM) and atomic force microscopy (AFM). In particular, slag-blended cement pastes were investigated using coupled TEM and electron microprobe analysis to demonstrate that the resulting inner products resulting from slag hydration are intimately mixed with Mg, Al-rich hydroxide phase, whereas the outer products are the same as the ones resulting from clinker hydration [3]. TGA was used to demonstrate the latent hydraulic properties of slag as decreasing combined water with slag replacement ratio was observed [4]. XRD analysis showed the formation of hydrotalcite and sjögrenite as main crystalline phases in cement-slag system [5], and coupling with the selective dissolution method made it possible to quantify the amount of CSH and unreacted amorphous slag in the total amorphous phase [6].

In the last decades, nanoindentation has been used in order to improve the current understanding of the microstructure features governing the mechanical behavior of cement pastes. For instance, this technique has been used to expand the knowledge about individual cement paste phases properties and contributions [7–10], as well as the impact of mineral admixtures incorporation [11–13]. For slag-based cementitious materials, a significantly increased porosity was measured at 7 days with a low-density CSH dominance [14]. Even after 3 months, a shift towards lower micromechanical properties was still observed [15]. Moreover, at 4 years hydration age, it was found that the volume fraction of all CSH morphologies (LD, HD and UHD) increases compared to Portland cement [16]. Nevertheless, the micromechanical investigation of early age (2 days) is still not addressed, especially regarding the viscoelastic properties of the binding phases.

In particular, the validity of statistical deconvolution techniques is sometimes questionable. For example, the least square error method was found to fit the probability density function better when taking into account few phases (2 or 3) of the cement paste. However, this situation does not reflect the blended cement pastes' actual compositions, and it can be hard to find the global optimum [17]. Some other studies used the maximum likelihood estimation method [12,18–21], which outputs clusters of mixtures of phases rather than pure ones. In order to adequately disclose the properties of individual phases, indentation was coupled to imaging techniques to refine statistical deconvolution results. Optical microscopic images of microindented areas were used to reduce the variability of the micromechanical properties associated with the indented phases [22]. Similarly, some authors have used a coupling with SEM-EDS analyses to assess the micromechanical signature of natural pozzolan incorporation in concrete [23].

This study focuses on the nanoindents' observation using SEM imaging and the effect of slag incorporation at the early age on elastic and contact creep modulus was investigated. With this aim, four cement pastes with different replacement ratios of Portland cement with slag were probed using instrumented nanoindentation. Then, backscattered electron micrographs of the indented areas were captured to observe indents in the individual paste phases closely, and explanations about some deconvolution problems were given.

2 Materials and Methods

2.1 Materials and sample preparation

In this experimental work, the water-to-binder ratio was kept constant at 0.3. The reference sample P_0 was manufactured using a CEM I 52.5 N cement. Slag was then incorporated to replace cement (by volume) by 30%, 45% and 60% (respectively labelled as PS_{30}, PS_{45} and PS_{60}). These two latter cement blends (PS_{45} and PS_{60}) are equivalent to the commercialized CEM III/A. The chemical compositions of the used materials are given in Table 1. Superplasticizer was used up to 0.5% to adjust some cement pastes fluidity. 4 x 4 x 16 cm^3 samples were cast, covered with plastic foil and cured at 20°C and 50% relative humidity. After 24h, the samples were demolded and kept in lime-saturated water until testing to avoid calcium leaching.

Table 1. Chemical and physical properties of used materials

		Cement	Slag
Chemical composition (%)	SiO_2	20.4	37.7
	Al_2O_3	4.4	10.2
	Fe_2O_2	2.3	0.6
	TiO_2	-	0.7
	CaO	64.0	43.8
	MgO	3.9	6.4
	SO_3	2.9	0.1
	K_2O	0.66	0.28
	Na_2O	0.15	0.21
	P_2O_5	0.1	-
	Cl^-	0.02	0.02
	S^{2-}	<0.02	0.7
	Na_2O eq.	0.58	0.44
Physical properties	Specific gravity (g/cm^3)	3.15	2.9
	Specific area (cm^2/g)	3979	4450

At 2 days of hydration, central cubes of 1 x 1 x 1 cm^3 were sawn, and hydration was stopped using the solvent exchange method with isopropanol. Then, they were im-

pregnated in resin and polished using abrasive papers and diamond pastes until a smooth surface was reached. Surface quality was assessed using the nanoindenter Scanning Probe Microscopy (SPM) mode using a Berkovich tip for surface mapping to calculate the Root-Mean-Square (RMS) roughness. These samples are to be used for nanoindentation and SEM imaging (further detailed), so a special care was given to the preparation step, to obtain data that are more accurate and facilitate the work on SEM images.

2.2 Experimental testing

Nanoindentation was performed using a Bruker TS 77 Berkovich to assess the micromechanical properties of the pastes individual phases under a force control mode. Target grids composed of 16 x 25 indents, spaced by 15 µm were performed, under a maximum load P_{max} = 2 mN kept constant for 60 s to measure creep. A marker grid of indents performed under 10 mN was also performed to help locating the target grid in SEM imaging (detailed further).

For the aim of this study, a precise tip-to-optic calibration is required. The calculation of micromechanical properties was done on the target grids. Reduced modulus E_r, elastic modulus E and hardness H were calculated using the formulas below:

$$E_r = \frac{1}{2}\sqrt{\frac{\pi}{A_c}}S \tag{1}$$

$$\frac{1}{E_r} = \frac{1-\nu^2}{E} + \frac{1-\nu_{ind}^2}{E_{ind}} \tag{2}$$

$$H = \frac{P_{max}}{A_c} \tag{3}$$

Where S is the slope of the unloading curve at maximum load, A_c is the projected contact area quantified using Oliver and Pharr approach [24] after a calibration of area function on quartz, ν is the cement paste Poisson's ratio which is equal to 0.24 [25], and $\nu_{ind} = 0.07$ and $E_{ind} = 1141$ GPa are respectively the diamond indenter Poisson's ratio and elastic modulus.

Contact creep modulus was evaluated using a logarithmic fit of the variation of penetration depth as follows:

$$\Delta h(t) = x_1 \ln(1 + x_2 t) \tag{4}$$

$$C = \frac{P_{max}}{2x_1\sqrt{A_c/\pi}} \tag{5}$$

Using a JEOL JSM-6060LA scanning electron microscope (SEM), the indented areas were located using the marker matrix that was performed near the target matrix with a known distance. In the following, the results from one target matrix of 400 indents per sample will be presented. The polished sections were studied in backscattered electron (BSE) mode at an acceleration voltage of 20 kV and a working distance of 7 mm. Small images with magnification x2000 were collected and stitched to achieve a satis-

ficing resolution (1 pixel = 50 nm) that enables the detection of some indents location to accurately deduce the others.

3 Results and Discussion

3.1 Micromechanical properties of individual phases observed in SEM images

Fig. 1 displays the BSE micrographs of some parts from target matrices where the indents could be located and seen and fig. 2 shows their load-depth and displacement change curves. Indents from different phases that could be seen in BSE images were selected and the measured elastic modulus, hardness and contact creep modulus were listed in table 2. The minimum and maximum penetration depth recorded from these indents are respectively about 104 nm in unhydrated clinker particle (fig. 1d, indent #9) and about 361 nm in outer products (fig. 1c, indent #4). From fig. 2a, and table 2, it can be noticed that the contact creep modulus value obtained during each nanoindentation test is generally opposite to the displacement change during the holding stage: the larger the contact creep modulus of the phase, the smaller the corresponding displacement change, highlighting a better capacity of the phase to resist creep deformation.

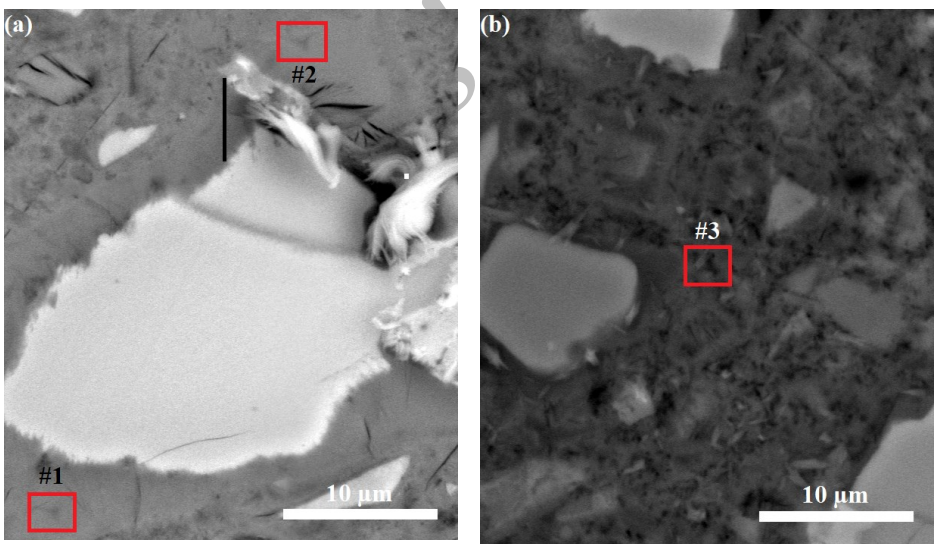

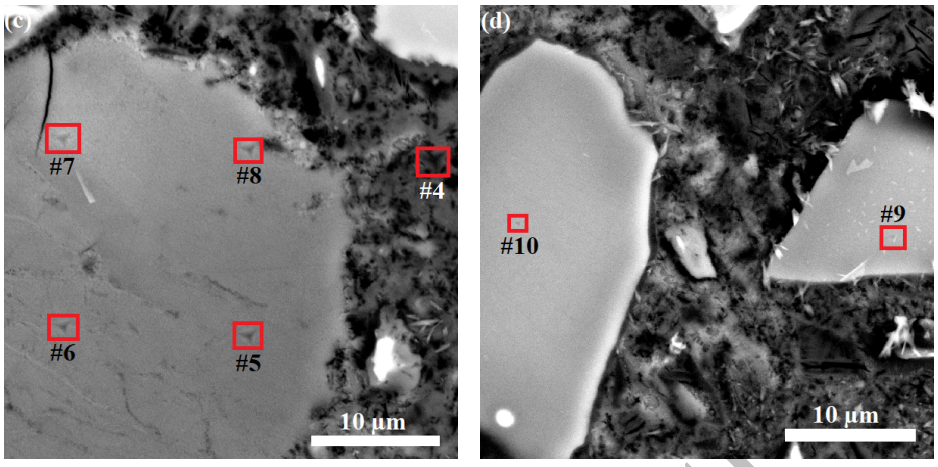

Fig. 1. BSE micrographs of visible indents framed in red boxes in (a) inner products (IP), (b) outer products (OP), (c) (OP) & portlandite (CH) and (d) unhydrated clinker (UC).

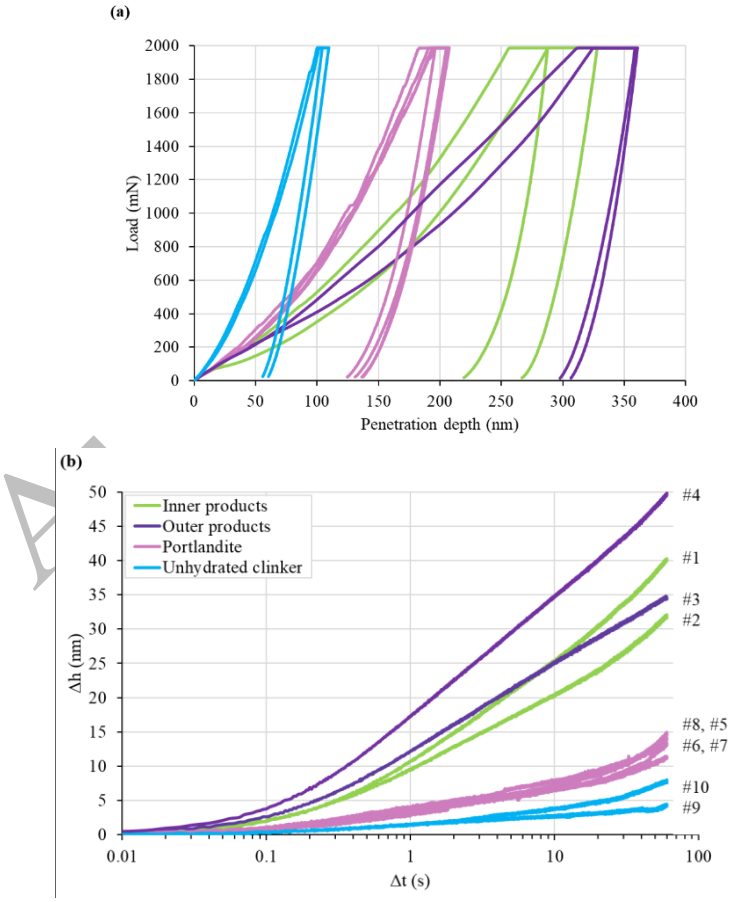

Fig. 2. (a) Load-depth curves and (b) creep curves of the visible indents showed in fig. 1.

Table 2. Micromechanical properties of the visible indents showed in fig. 1.

Indent ref.	Phase	E (GPa)	H (GPa)	C (GPa)
#1	IP	32.81	0.97	158.12
#2		40.62	1.09	223.03
#3	OP	25.53	0.66	185.35
#4		30.07	0.64	360.80
#5	CH	43.81	2.09	647.08
#6		49.38	2.3	609.46
#7		42.84	2.12	812.71
#8		44.49	2.13	491.74
#9	UC	106.93	8.13	5532.00
#10		101.16	7.33	1532.84

In fig. 1a, inner products within the boundaries of the original clinker grain can be easily distinguished, and two indents #1 and #2 can be located. According to their calculated properties, indent #1 belongs to HD (high-density) CSH phase and that indent #2 is within a UHD phase (ultra high-density, which is a composition of CSH and CH) [26]. Fig. 1b and 1c show two indents in outer products where the recorded penetration depth was maximal, according to fig. 2a. The values of E and H are consistent with the values recorded in [27] for outer products, and the values of C are different but are still in the range of CSH and UHD phase, according to [26]. As shown in fig. 2b, OP experiences more creep than IP at the beginning, but this changes after the 10 s creep and affects the value of the contact creep modulus. This may be due to two reasons: the first is the thermal drift that becomes more important with a longer load-holding stage, and the second is the probable change of phase with longer creep experiment.

Four indents in a pure portlandite particle are shown in fig. 1c where the mean properties are 45.13 $\pm$ 2.91 GPa for elastic modulus, 2.16 $\pm$ 0.09 GPa for hardness and 640 $\pm$ 132.65 GPa for contact creep modulus which are consistent with the values found in [9]. After 60 s of creep, the deformation in portlandite represents practically one-third of that of CSH phases (14 nm in average compared to 40 nm for IP and OP) and thus it should be taken into account when analyzing the creep behavior of concretes. Indent #8 shows a low contact creep modulus compared to the other indents inside the portlandite particle. This might be due to the boundary conditions of the indented area: this particular indent is near a small CSH phase which creeps more than portlandite. Thus, special attention should be given to the values of micromechanical properties measured near boundaries between different phases. This also may

suggest that the thickness of the indented particle and the nature of the phase below influence on the measured properties.

Despite their shallow penetration, indents in unhydrated particles could be seen, as shown in fig. 1d, and the found properties are in agreement with the ones reported in the literature [27]. As shown in fig. 2b, the creep of unhydrated clinker particles is not significant compared to hydration products, which means that the logarithmic fit does not necessarily describe its behavior, which induces significant differences in their creep properties.

3.2 Influence of slag incorporation on micromechanical properties of the paste

Fig. 3 shows the probability density function of the elastic modulus and contact creep modulus for the four cement pastes at 2 and 28 days of hydration. They were limited to respectively 60 GPa and 600 GPa to analyze only hydration products' properties. At 2 days, the main hydration peak for the reference mix for elastic modulus is at 34 GPa, which is characteristic of a HD CSH dominant cement paste with a small peak around 46 GPa, typical of portlandite. The same observation can be done for the main hydration peak of PS_{30}, but the peak is larger to cover more values from LD CSH. When increasing the slag replacement ratio to 45%, the main peak shifts to lower elastic modulus of 30 GPa with a visible peak around 40 GPa. Finally, with 60% cement replacement, the main hydration peak was reduced of about 30% compared to the reference mix, with the domination of LD CSH values and a much lower fraction of HD CSH, and a minor number of indents observed in portlandite.

Overall, we notice that elastic modulus decreases with the slag replacement ratio at early age. Indeed, slag is a hydraulic latent mineral addition and is less reactive than CEM I in the first hours of hydration, as it needs an alkaline environment and calcium from calcium hydroxide coming from cement grains hydration to react. In addition, the amount of hydrated slag was found to decrease for increased slag incorporation ratio and decreased water-to-binder ratio. For a an order of magnitude, a mix with 30% of slag, with a w/b=0.35 cured at 30°C has an amount of reacted slag at 3 days of about 7.5% [28]. Therefore, the amount of formed CSH in the cement blends decreases with slag replacement ratio because of the lowest amount of cement in the mix in one hand and the lowest amount of CSH coming from slag hydration on the other hand. Later after 28 days of hydration, the elastic modulus of highest peaks seem to be the same of 30 GPa. However, the peaks of hydration products elastic modulus are slightly narrower and show bimodal distribution to indicate the formation of portlandite and/or UHD phase.

(a)

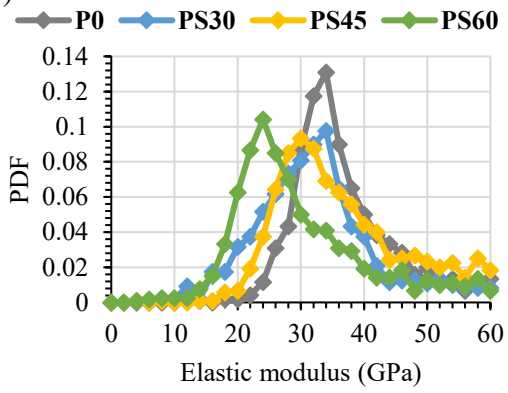
P0
PS30
PS45
PS60
PDF
0.14
0.12
0.1
0.08
0.06
0.04
0.02
0
0
10
20
30
40
50
60
Elastic modulus (GPa)

(b)

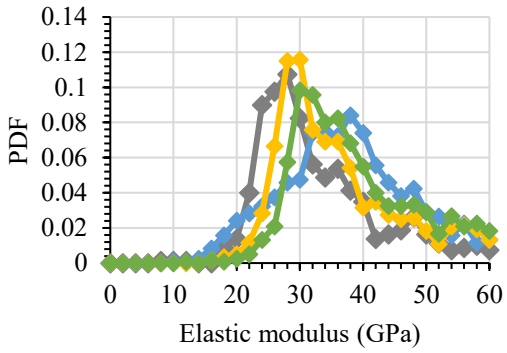
PDF
0.14
0.12
0.1
0.08
0.06
0.04
0.02
0
0
10
20
30
40
50
60
Elastic modulus (GPa)

(c)

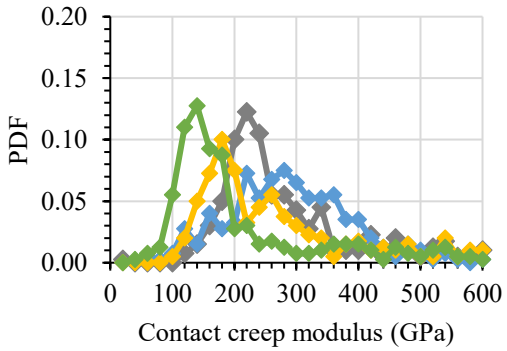
PDF
0.20
0.15
0.10
0.05
0.00
0
100
200
300
400
500
600
Contact creep modulus (GPa)

(d)

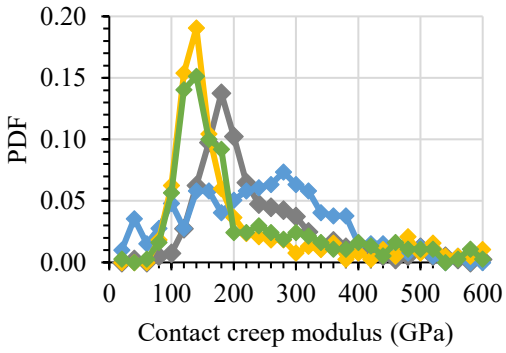

Fig. 3. Probability density function of the four cement pastes for elastic modulus at (a) 2 days, (b) 28 days (bin size of 2 GPa) and contact creep modulus at (c) 2 days, (d) 28 days (bin size of 20 GPa).

As for contact creep modulus at early age, P_0 shows a main peak at C = 220 GPa which is characteristic for HD CSH with a smaller peak towards at 320 GPa for an UHD phase. When 30% of slag is incorporated, the distribution of contact creep modulus becomes larger and covers the whole range of hydration products modulus. The incorporation of 45% and 60% of slag causes a shift of the main peak towards decreased modulus at respectively 180 GPa and 140 GPa. Meanwhile, a second peak is observed in PS_{45} and PS_{60} at respectively 260 GPa 180 GPa which is characteristic of HD CSH but no UHD phase nor portlandite was detected. The porosity of hydration products issued from the binders hydration seems to be the major factor affecting the observed distribution of contact creep modulus. Later at 28 days, the same observations could be done but with more LD CSH observed in PS_{45} and PS_{60}. Indeed, the incorporation of slag increases the gel porosity and porosity enables more deformation for hydration products, which results in a reduced contact creep modulus.

4 Conclusion

In this study, the nanoindentation technique was used to assess the effect of slag incorporation in cement pastes at early and advanced ages using four binary systems with different replacement ratios by slag. In addition, scanning electron microscopy was used to address some issues encountered in nanoindentation data deconvolution. The observed discrepancy in micromechanical properties of inner and outer products, as well as of portlandite shows that the hydration products are intimately intermixed and that boundary conditions of the indented areas impact the measured properties and thus deconvolution process. In addition, a reduction in elastic modulus and contact creep modulus with cement replacement ratio with slag was demonstrated due to increased gel porosity with slag incorporation at early age. This observation is con-

firmed at 28 days on the viscoelastic behavior of the cement blends with higher amounts of porous hydration products.

The use of SEM to locate and eliminate the indents that are affected by the boundary conditions can be a powerful tool to supply some sophisticated micromechanical models with more accurate input data and thus produce results of better precision.

References

[1] J. Ambroise, S. Maximilien, J. Pera, Properties of Metakaolin blended cements, Advanced Cement Based Materials. 1 (1994) 161–168. https://doi.org/10.1016/1065-7355(94)90007-8.

[2] V.G. Papadakis, E.J. Pedersen, H. Lindgreen, An AFM-SEM investigation of the effect of silica fume and fly ash on cement paste microstructure, Journal of Materials Science. 34 (1999) 683–690. https://doi.org/10/bnvqr6.

[3] I.G. Richardson, G.W. Groves, Microstructure and microanalysis of hardened cement pastes involving ground granulated blast-furnace slag, J Mater Sci. 27 (1992) 6204–6212. https://doi.org/10.1007/BF01133772.

[4] B. Kolani, L. Buffo-Lacarrière, A. Sellier, G. Escadeillas, L. Boutillon, L. Linger, Hydration of slag-blended cements, Cement and Concrete Composites. 34 (2012) 1009–1018. https://doi.org/10.1016/j.cemconcomp.2012.05.007.

[5] M. Boháč, M. Palou, R. Novotný, J. Másilko, D. Všianský, T. Staněk, Investigation on early hydration of ternary Portland cement-blast-furnace slag–metakaolin blends, Construction and Building Materials. 64 (2014) 333–341. https://doi.org/10.1016/j.conbuildmat.2014.04.018.

[6] S. Hoshino, K. Yamada, H. Hirao, XRD/Rietveld Analysis of the Hydration and Strength Development of Slag and Limestone Blended Cement, ACT. 4 (2006) 357–367. https://doi.org/10.3151/jact.4.357.

[7] G. Constantinides, F.-J. Ulm, The nanogranular nature of C–S–H, Journal of the Mechanics and Physics of Solids. 55 (2007) 64–90. https://doi.org/10.1016/j.jmps.2006.06.003.

[8] L. Sorelli, G. Constantinides, F.-J. Ulm, F. Toutlemonde, The nano-mechanical signature of Ultra High Performance Concrete by statistical nanoindentation techniques, Cement and Concrete Research. 38 (2008) 1447–1456. https://doi.org/10.1016/j.cemconres.2008.09.002.

[9] D. Davydov, M. Jirásek, L. Kopecký, Critical aspects of nano-indentation technique in application to hardened cement paste, Cement and Concrete Research. 41 (2011) 20–29. https://doi.org/10.1016/j.cemconres.2010.09.001.

[10] C. Hu, Z. Li, A review on the mechanical properties of cement-based materials measured by nanoindentation, Construction and Building Materials. 90 (2015) 80–90. https://doi.org/10/gd8436.

[11] S. Barbhuiya, P. Chow, S. Memon, Microstructure, hydration and nanomechanical properties of concrete containing metakaolin, Construction and Building Materials. 95 (2015) 696–702. https://doi.org/10.1016/j.conbuildmat.2015.07.101.

[12] H. Chualin, L. Zongjin, Property investigation of individual phases in cementitious composites containing silica fume and fly ash, Cement and Concrete Composites. 57 (2015) 17–26. https://doi.org/10.1016/j.cemconcomp.2014.11.011.

[13] D. Damidot, K. Velez, F. Sorrentino, CHARACTERISATION OF INTERSTITIAL TRANSITION ZONE (ITZ) OF HIGH PERFORMANCE CEMENT BY NANOINDENTATION TECHNIQUE, (n.d.) 11.

[14] N. Shanahan, A. Markandeya, A. Elnihum, Y.P. Stetsko, A. Zayed, Multi-technique investigation of metakaolin and slag blended portland cement pastes, Applied Clay Science. 132–133 (2016) 449–459. https://doi.org/10.1016/j.clay.2016.07.015.

[15] C. Hu, Z. Li, Y. Gao, Y. Han, Y. Zhang, Investigation on microstructures of cementitious composites incorporating slag, Advances in Cement Research. 26 (2014) 222–232.

[16] F. Han, Z. Zhang, Micromechanical properties of 4-year-old composite binder pastes with different mineral admixtures using nanoindentation technique, Journal of Building Engineering. 61 (2022) 105264. https://doi.org/10.1016/j.jobe.2022.105264.

[17] P. Lura, P. Trtik, B. Münch, Validity of recent approaches for statistical nanoindentation of cement pastes, Cement and Concrete Composites. 33 (2011) 457–465. https://doi.org/10/cbnjk3.

[18] F.-J. Ulm, M. Vandamme, H.M. Jennings, J. Vanzo, M. Bentivegna, K.J. Krakowiak, G. Constantinides, C.P. Bobko, K.J. Van Vliet, Does microstructure matter for statistical nanoindentation techniques?, Cement and Concrete Composites. 32 (2010) 92–99. https://doi.org/10/cq28qh.

[19] S. Al-Shmaisani, R.D. Kalina, R.D. Ferron, M.C.G. Juenger, Critical assessment of rapid methods to qualify supplementary cementitious materials for use in concrete, Cement and Concrete Research. 153 (2022) 106709. https://doi.org/10.1016/j.cemconres.2021.106709.

[20] R.J. Thomas, B.S. Gebregziabiher, A. Giffin, S. Peethamparan, Micromechanical properties of alkali-activated slag cement binders, Cement and Concrete Composites. 90 (2018) 241–256. https://doi.org/10.1016/j.cemconcomp.2018.04.003.

[21] Z. Luo, W. Li, Y. Gan, K. Mendu, S.P. Shah, Applying grid nanoindentation and maximum likelihood estimation for N-A-S-H gel in geopolymer paste: Investigation and discussion, Cement and Concrete Research. 135 (2020) 106112. https://doi.org/10.1016/j.cemconres.2020.106112.

[22] B. Hilloulin, M. Robira, A. Loukili, Coupling statistical indentation and microscopy to evaluate micromechanical properties of materials: Application to viscoelastic behavior of irradiated mortars, Cement and Concrete Composites. 94 (2018) 153–165. https://doi.org/10/ghdf49.

[23] W. Wilson, J.M. Rivera-Torres, L. Sorelli, A. Durán-Herrera, A. Tagnit-Hamou, The micromechanical signature of high-volume natural pozzolan concrete by combined statistical nanoindentation and SEM-EDS analyses, Cement and Concrete Research. 91 (2017) 1–12. https://doi.org/10.1016/j.cemconres.2016.10.004.

[24] W.C. Oliver, G.M. Pharr, An improved technique for determining hardness and elastic modulus using load and displacement sensing indentation experiments, Journal of Materials Research. 7 (1992) 1564–1583. https://doi.org/10/bdv47f.

[25] G. Constantinides, F.-J. Ulm, The effect of two types of C-S-H on the elasticity of cement-based materials: Results from nanoindentation and micromechanical modeling, Cement and Concrete Research. 34 (2004) 67–80. https://doi.org/10.1016/S0008-8846(03)00230-8.

[26] M. Vandamme, F.-J. Ulm, Nanoindentation investigation of creep properties of calcium silicate hydrates, Cement and Concrete Research. 52 (2013) 38–52. https://doi.org/10/f5f4zk.

[27] C. Hu, Nanoindentation as a tool to measure and map mechanical properties of hardened cement pastes, MRS Communications. 5 (2015) 83–87. https://doi.org/10.1557/mrc.2015.3.

[28] J.I. Escalante, L.Y. Gómez, K.K. Johal, G. Mendoza, H. Mancha, J. Méndez, Reactivity of blast-furnace slag in Portland cement blends hydrated under different conditions, Cement and Concrete Research. 31 (2001) 1403–1409. https://doi.org/10.1016/S0008-8846(01)00587-7.